Journal of Alloys and Compounds 511 (2012) 215–220

Contents lists available at SciVerse ScienceDirect

Journal of Alloys and Compounds

journal homepage: www.elsevier.com/locate/jallcom

Surface vitrification of alloys by laser surface treatment

Bingqing Chen [a], Yan Li [a], Yan Cai [b], Ran Li [a], Shujie Pang [a], Tao Zhang [a,*]

[a] *Key Laboratory of Aerospace Materials and Performance (Ministry of Education), School of Materials Science and Engineering, Beihang University, 100191 Beijing, China*
[b] *School of Aeronautic Science and Engineering, Beihang University, 100191 Beijing, China*

ARTICLE INFO

Article history:
Received 26 July 2011
Received in revised form
12 September 2011
Accepted 14 September 2011
Available online 19 September 2011

Keywords:
Laser
Metallic glasses
Microstructure
Glass-forming ability
Thermal simulation

ABSTRACT

With laser surface treatment (LST) method, the surfaces of Zr-, Cu-, Fe- and Al-based alloys were melted and amorphous or amorphous–crystalline composite structures were synthesized, which were related to the different glass-forming ability of the alloys. Influences of laser processing parameters on glass formation for $Cu_{60}Zr_{30}Ti_{10}$ alloy were investigated and the laser treated alloy exhibited a gradient structure: amorphous surface, amorphous–crystalline composites transitional region and crystalline substrate. Temperature distributions and thermal profiles of the treated $Cu_{60}Zr_{30}Ti_{10}$ alloy during the laser process were simulated using finite volume method. The formation mechanism of the gradient structure is discussed based on the experimental and simulated results.

1. Introduction

Due to the high hardness, high corrosion resistance and structural uniformity, bulk metallic glasses (BMGs) can be a good candidate for anti-wear and corrosion resistance coatings on metallic components [1–4]. Laser surface treatment (LST) is a feasible technique to produce metallic glass surface/coatings since the cooling rates during laser processing can achieve 10^5–10^8 K/s, much higher than the critical cooling rates (R_c) of BMGs with good glass-forming ability (GFA) [5,6]. Studies on the synthesis of metallic glasses by LST including laser surface melting and laser powder cladding have been performed. For the alloy systems with low GFA, amorphous surfaces synthesized by laser processing were only restricted to thin films [7–9]. Recently, amorphous surface layers with relatively large thickness have been synthesized in Zr-based alloys with high GFA [10,11]. With high laser power density, amorphous surface coatings of Cu-, Fe-, Ni- and Zr-based alloys have also been prepared using laser powder cladding method [12–16]. The production of metallic glasses in the form of coatings or surface layers by LST is considered to be an interesting technological achievement for the wide range of applications in which wear and corrosion resistance is a main requirement, and the amorphous surface coatings exhibit optimized mechanical properties than the crystalline substrates [5,11–13,16]. For the glass formation by LST, several issues are critical and under investigation: (1) the influences of GFA of alloys and laser processing parameters on the synthesis of amorphous surfaces, (2) the microstructure profile along the laser-affected depth subjected to different thermal influences during the LST, and (3) the mechanism of laser induced microstructure evolution in thermodynamic and kinetics aspects. In this work, Zr-, Cu-, Fe- and Al-based crystalline substrates were treated by laser surface melting and the formation of amorphous surface layers were investigated in terms of their significant disparity in GFA. The influences of laser scanning speed and working voltage on the glass formation of $Cu_{60}Zr_{30}Ti_{10}$ alloy were studied. The treated $Cu_{60}Zr_{30}Ti_{10}$ alloy exhibited gradient microstructure: amorphous surface, amorphous–crystalline composites transitional region and crystalline substrate. Based on the experimental and thermal simulated results, the formation mechanism of the gradient microstructure is discussed in terms of the thermodynamic and kinetic factors.

2. Experimental

Alloy ingots with nominal compositions of $Zr_{55}Al_{10}Ni_5Cu_{30}$, $Zr_{48}Cu_{40}Al_{10}Y_2$, $Cu_{60}Zr_{30}Ti_{10}$, $Cu_{64}Zr_{36}$, $[(Fe_{0.5}Co_{0.5})_{0.75}B_{0.2}Si_{0.05}]_{96}Nb_4$, $Al_{86}Si_{0.5}Ni_{4.06}Co_{2.94}Y_6Sc_{0.5}$, and $Al_{85}Ni_5Y_{10}$ (at.%) were prepared by arc-melting the mixture of the pure elements under a Ti-gettered, purified argon atmosphere. The ingots were turned over and remelted at least 4 times to insure the compositional homogeneity. Rectangular plates of 2 mm in thickness, 10 mm in width and 10 mm in length for laser treatment were machined from the ingots. The plates were polished with 2000-grit SiC papers followed by cleaning and degreasing with distilled water and acetone. Laser melting treatment on the surfaces of the plates was carried out using an Nd: YAG laser with the focused beam diameter of 1 mm, pulse frequency of 8 Hz and pulse width of 1 ms at various beam scanning speeds and laser working voltages. During the laser process, an Ar flow was used to prevent surface oxidation. Parallel tracks

---

* Corresponding author. Tel.: +86 1082316192.
E-mail address: zhangtao@buaa.edu.cn (T. Zhang).

0925-8388/$ – see front matter
doi:10.1016/j.jallcom.2011.09.039

with partial overlapping (~50%) were laid with the focused circular spots of 1 mm in diameter on the surfaces of the substrate plates.

Structures of the top surfaces of the treated plates were examined by X-ray diffractometer (XRD) (Bruke D8-advance). For the treated $Cu_{60}Zr_{30}Ti_{10}$ alloy, various layers from the top surface to the crystalline substrate were subjected to the XRD examinations in the plane view, which were obtained by mechanical polishing the top surfaces to certain depths. The cross sections of the $Cu_{60}Zr_{30}Ti_{10}$ alloys treated with different processing parameters were observed by scanning electron microscopy (SEM) (CS-3400). Microhardness depth profile was measured by Vickers hardness tester (450-SVD) along the depth from the top surface of the treated $Cu_{60}Zr_{30}Ti_{10}$ alloy at a load of 500 g applied for 15 s, and at least 20 indents were performed at each position. The density of the $Cu_{60}Zr_{30}Ti_{10}$ alloy was measured with the Archimedes method.

3. Results and discussion

The surfaces of the Zr-, Cu-, Fe- and Al-based alloys were treated at various beam scanning speeds and laser working voltages, and the optimum processing parameters for surface vitrification of each alloy were determined. Fig. 1 shows the XRD patterns of the top surfaces of the Zr-, Cu-, Fe- and Al-based alloys treated with their optimum laser processing parameters, respectively. Thermal properties and critical diameters (D_c) of these glassy alloys [17–23] are summarized in Table 1. In the XRD patterns of $Zr_{55}Al_{10}Ni_5Cu_{30}$, $Zr_{48}Cu_{40}Al_{10}Y_2$, and $Cu_{60}Zr_{30}Ti_{10}$ alloys, a broad diffraction maxima without any detectable sharp Bragg peak is observed, indicating the amorphous structures. The XRD patterns of $[(Fe_{0.5}Co_{0.5})_{0.75}B_{0.2}Si_{0.05}]_{96}Nb_4$, $Cu_{64}Zr_{36}$, and $Al_{86}Si_{0.5}Ni_{4.06}Co_{2.94}Y_6Sc_{0.5}$ alloys show α-Fe, $Cu_{10}Zr_7$, and fcc-Al crystalline peaks, respectively, besides a broad maxima. For the treated $Al_{86}Si_{0.5}Ni_{4.06}Co_{2.94}Y_6Sc_{0.5}$ alloy, the existence of amorphous phase on the surface is further confirmed by the differential scanning calorimetry (DSC) curve which exhibits a heat release peak corresponding to the crystallization of amorphous phase. The $Al_{85}Ni_5Y_{10}$ alloy is still crystalline after laser treated. It is indicated that, in general, the alloys with higher GFA show stronger glass-forming tendency by laser surface melting. The experimental results reveal that amorphous surface layers can be easily formed on the Zr-based alloys by laser surface melting over a wide range of processing parameters, which is due to their high GFA evidenced by the centimeter class D_c. Though the D_c of $Cu_{60}Zr_{30}Ti_{10}$ alloy is much smaller than those of the Zr-based alloys, the alloy also shows amorphous structure on the surface after the laser treatment. For $Cu_{60}Zr_{30}Ti_{10}$ alloy, the surface structure induced by laser is sensitive to the change of processing parameters, which are limited in a narrow range for amorphous structure to form. This also makes the $Cu_{60}Zr_{30}Ti_{10}$ alloy suitable for studying the effect of laser processing parameters on glass formation. In comparison with $Cu_{60}Zr_{30}Ti_{10}$ alloy, the $[(Fe_{0.5}Co_{0.5})_{0.75}B_{0.2}Si_{0.05}]_{96}Nb_4$ alloy owns larger D_c, while the precipitation of crystalline α-Fe on the surface after laser treated is found. It is considered that, since the laser heating duration is limited, some cells possibly cannot be melted and transitorily remain in the melted region, especially for the alloys with high melting temperatures such as the Fe-based alloy. These tiny cells can be the heterogeneous nucleation sites and the crystalline phases will precipitate and grow with low nucleation energy barrier. On the other hand, if the laser energy is too high, the thermal burden would increase which is also unfavorable to the glass formation. For $Cu_{64}Zr_{36}$, $Al_{86}Si_{0.5}Ni_{4.06}Co_{2.94}Y_6Sc_{0.5}$ and $Al_{85}Ni_5Y_{10}$ alloys, because of their relatively low GFA, amorphous surface cannot be formed by the laser surface melting in this work.

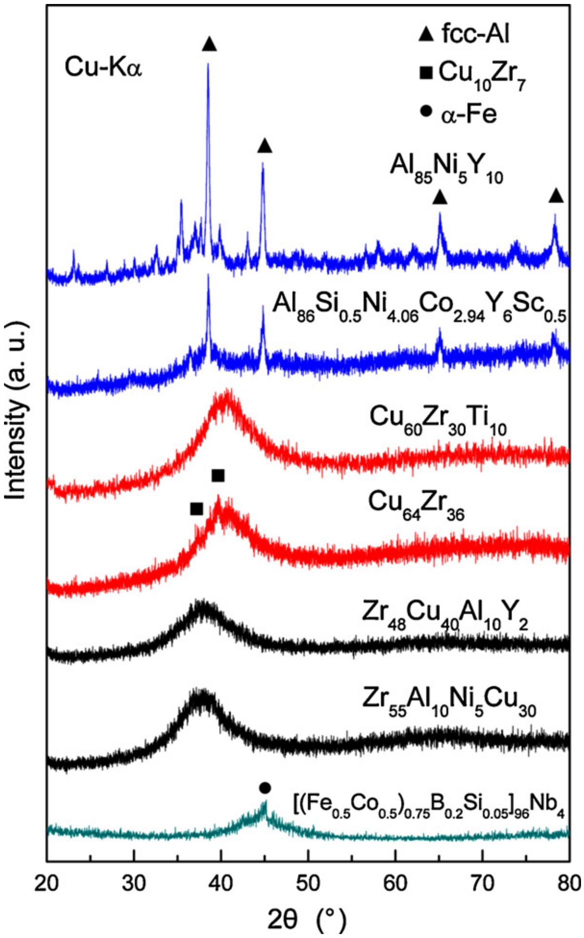

Fig. 1. XRD patterns of the top surfaces of the laser treated Zr-, Cu-, Fe- and Al-based alloys.

Besides the disparity in GFA and the melting temperatures, the compositional inhomogeneity in the crystalline ingots and microstructural nonuniformity among the untreated substrates for different alloys could have an effect on the surface microstructures induced by laser surface melting. Except for $Cu_{64}Zr_{36}$, the alloys investigated here are multicomponent alloys (more than 3 elements). Therefore, compositional inhomogeneity may exist as the segregation in the crystalline alloys, and the surface microstructures after laser treated would be influenced. On the other hand, though the $Zr_{55}Al_{10}Ni_5Cu_{30}$ ingot was confirmed as crystalline structure [11], the crystalline grains in the Zr-based alloys are fine due to their large GFA and the other crystalline alloys with

Table 1
Glass transition temperature (T_g), onset temperature of crystallization (T_x), solidus temperature (T_m), liquidus temperature (T_l) and critical diameters (D_c) of the Zr-, Cu-, Fe- and Al-based metallic glasses.

Alloy (at.%)	T_g (K)	T_x (K)	T_m (K)	T_l (K)	D_c (mm)	Ref.
$Zr_{55}Al_{10}Ni_5Cu_{30}$	685	774	1090	1156	10	[17]
$Zr_{48}Cu_{40}Al_{10}Y_2$	670	768	1040	1153	12	[18]
$Cu_{64}Zr_{36}$	787	833	1158	1223	2	[19]
$Cu_{60}Zr_{30}Ti_{10}$	724	746	1106	1175	4	[20]
$[(Fe_{0.5}Co_{0.5})_{0.75}B_{0.2}Si_{0.05}]_{96}Nb_4$	820	870	–	1390	5	[21]
$Al_{86}Si_{0.5}Ni_{4.06}Co_{2.94}Y_6Sc_{0.5}$	–	497	903	1055	~1	[22]
$Al_{85}Ni_5Y_{10}$	537	560	906	1249	<0.2	[23]

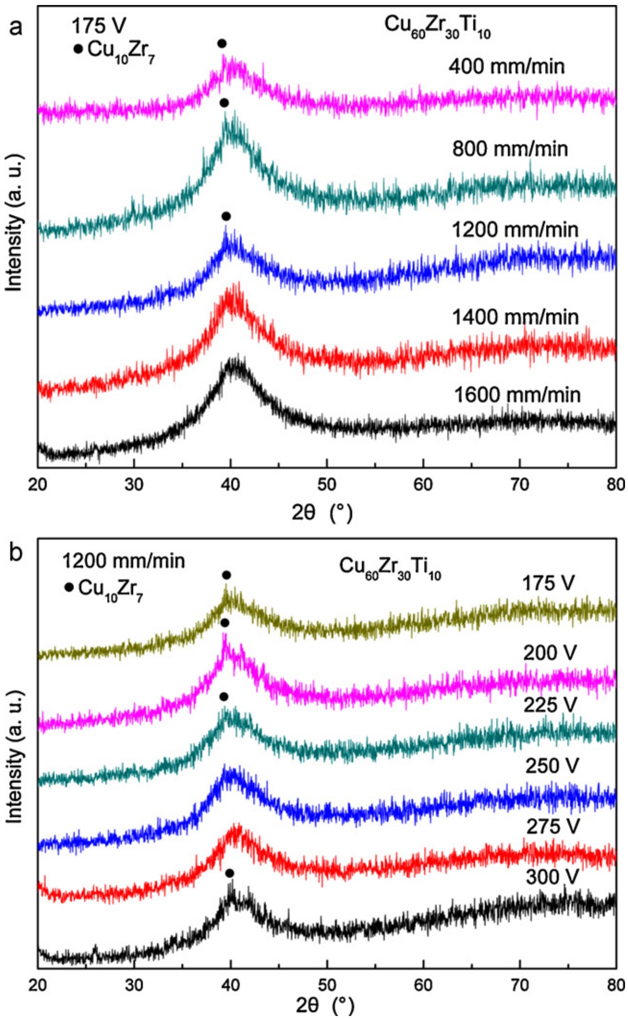

Fig. 2. XRD patterns of the $Cu_{60}Zr_{30}Ti_{10}$ alloy treated with different processing parameters: (a) working voltage is 175 V and scanning speed changes in the range of 400–1600 mm/min, (b) scanning speed is 1200 mm/min with working voltages from 175 V to 300 V.

relatively low GFA could contain coarse crystallites by comparison. In the process of laser melting, the melted region would be rapidly quenched by self-substrate chilling through thermal conduction and convection, so the substrate microstructures could affect the resultant surface structures. Furthermore, the laser pulse affected zone is relatively localized and the convection current in the molten pool can be different for various alloys and laser processing parameters, which could further induce nonuniform elements distributions [24].

Fig. 2 shows the XRD patterns of the $Cu_{60}Zr_{30}Ti_{10}$ alloys treated with different scanning speeds and working voltages. Firstly, the working voltage is fixed at 175 V and the scanning speed changes in the range of 400–1600 mm/min. As shown in Fig. 2(a), when the scanning speed is lower than 1400 mm/min, sharp Bragg peaks corresponding to $Cu_{10}Zr_7$ intermetallic phase are detected in the patterns. When treated at higher scanning speeds of 1400 mm/min and 1600 mm/min, the top surfaces are amorphous, which could be resulted from the enhanced cooling rates due to the increase in the intervals between the successive laser spots and the reduction of the annealing effects between each spot [15,25]. Secondly, when the scanning speed is fixed at 1200 mm/min, proper high working voltages are beneficial to the formation of amorphous structure. As seen in Fig. 2(b), when the working voltage is 175 V, 200 V and 225 V, the precipitations of $Cu_{10}Zr_7$ intermetallics are observed. When treated at higher working voltages of 250 V and 275 V, the surfaces exhibits amorphous structures. The results indicate that, though the relatively higher working voltages would induce higher temperatures and thicker melted layers and increase the thermal burden, the cooling rates are still high enough for amorphous structure to form. However, when the working voltage increases to 300 V, the alloy surface after laser treated is consisted of crystalline and amorphous phases. It is suggested that at this high voltage the melted region was enlarged and the temperature increased, so that the melted layer could not be cooled below the glass transition temperature (T_g) within the limited time and crystallization occurred.

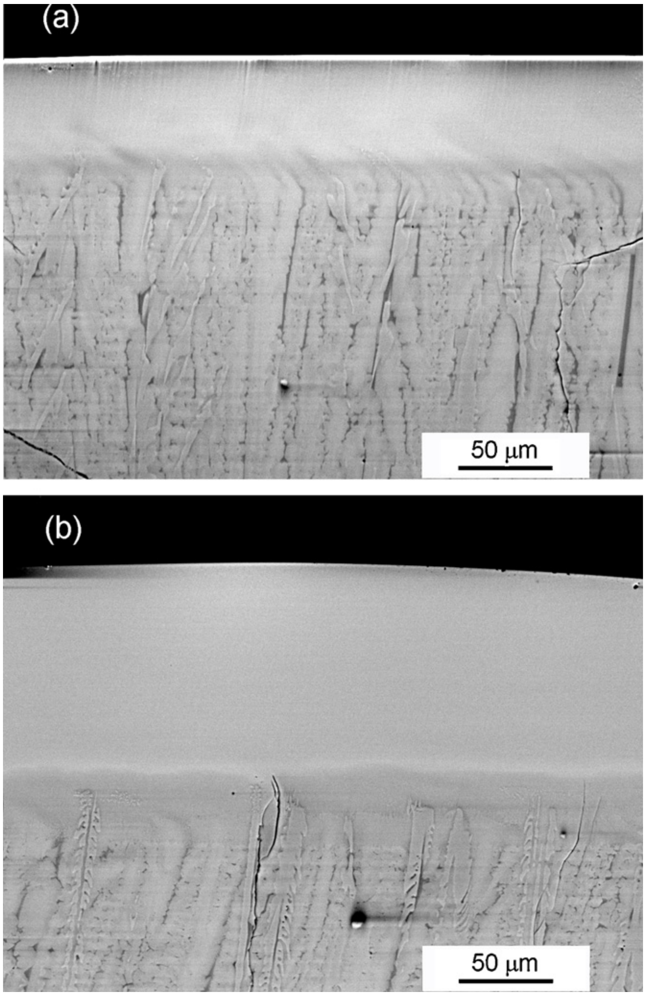

Fig. 3. SEM images of the cross-sections of the laser surface treated $Cu_{60}Zr_{30}Ti_{10}$ alloys. (a) working voltage of 175 V and scanning speed of 1200 mm/min, (b) working voltage of 250 V and scanning speed of 1200 mm/min.

Fig. 3(a) and (b) are the SEM back scattered images of the cross sections of the $Cu_{60}Zr_{30}Ti_{10}$ alloys treated at the scanning speed of 1200 mm/min, and the working voltages of 175 V and 250 V, respectively. The edge of the melted zone is clearly visible in the micrographs, and the thickness of the melted layer is around 80 μm at the voltage of 175 V and increases to 150 μm at the voltage of 250 V. The upper part of the melted zone exhibits featureless morphology, while the nether part reveals a relatively dark region where crystallites are seen. The crystalline substrate consists of developed dendrites, which disappear at the border to the melted zone. It is concluded that when a low working voltage is applied, the low laser power density will induce a thin melted region as illustrated in Fig. 3(a). Though the low energy decreases the thermal burden, crystals can nucleate and grow from the crystalline

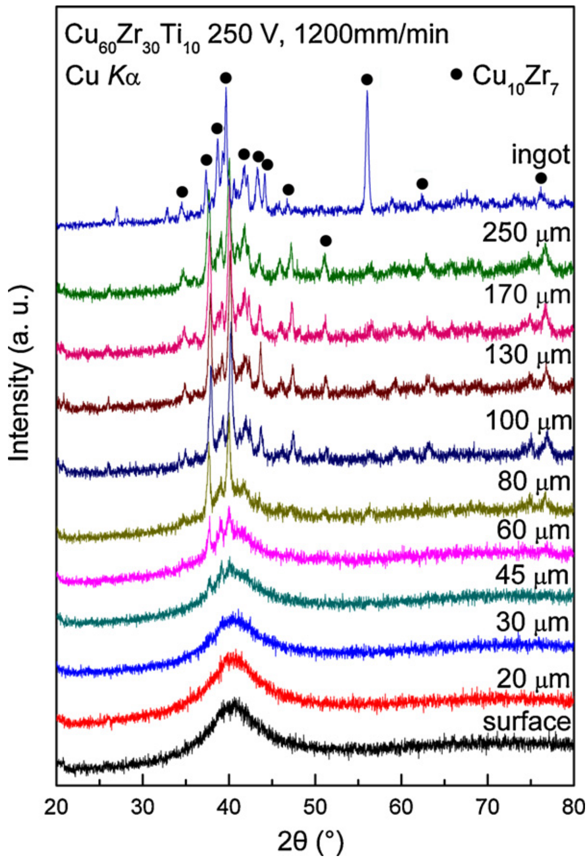

Fig. 4. XRD depth profile of the laser surface treated $Cu_{60}Zr_{30}Ti_{10}$ alloy.

substrate and easily pass through the thin melted layer to the top surface. In contrast, a thick melted layer induced by the proper high working voltage is beneficial to the formation of amorphous structure in the surface layer.

Fig. 4 shows the XRD patterns taken in the plane view at different depths from the top surface of the $Cu_{60}Zr_{30}Ti_{10}$ alloy treated at 250 V voltage and 1200 mm/min scanning speed, which indicate the continuously evolution of microstructure in depth direction. Combining the XRD results with the SEM images in Fig. 3, the laser treated $Cu_{60}Zr_{30}Ti_{10}$ alloy shows a gradient structure along the depth from the top surface towards the underneath substrate: amorphous surface (0–30 μm), composite layer consisted of ultrafine crystalline particles and amorphous phase (transitional layer A, 30–100 μm), composite layer containing dendrites and residual amorphous phase (transitional layer B, 100–150 μm) and crystalline substrate (>150 μm). Fig. 5 shows the SEM images taken from transitional layers A and B in the plane view. For transitional layer A, the XRD patterns exhibit crystalline peaks imposed on the halo, while contrast is hardly observed in the SEM images in Fig. 3(b) and Fig. 5(a), indicating the existence of ultrafine crystallites with low volume fraction in the amorphous matrix. Transitional layer B corresponds to the relatively dark region in Fig. 3(b). It can be clearly seen from Fig. 5(b), the transitional layer B shows dendrites and residual amorphous/ultrafine-crystalline phases composite structure. The dendrites exhibit more than 10 μm length for primary dendrite arms and large quantity in volume. Besides the dendrites grown from the nucleated particles after laser melting, part of the developed dendrites of the crystalline substrate could also be reserved, which were broken and stirred by the laser pulse and randomly distributed in the residual amorphous/ultrafine-crystalline phases.

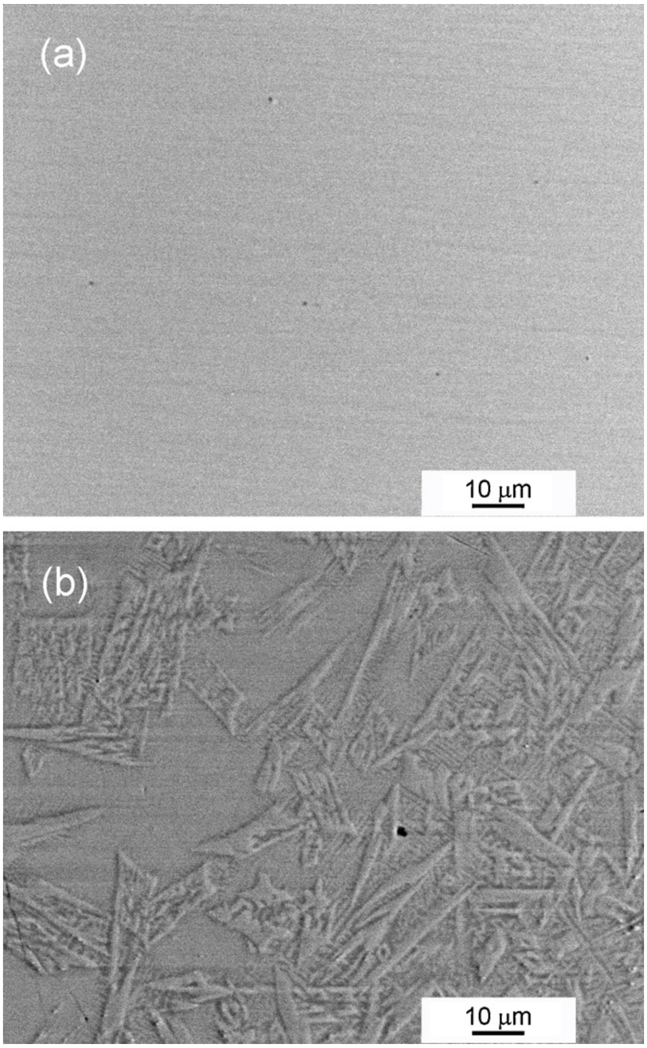

Fig. 5. SEM images taken from (a) transitional layer A and (b) transitional layer B in the plane view of the laser surface treated $Cu_{60}Zr_{30}Ti_{10}$ alloys.

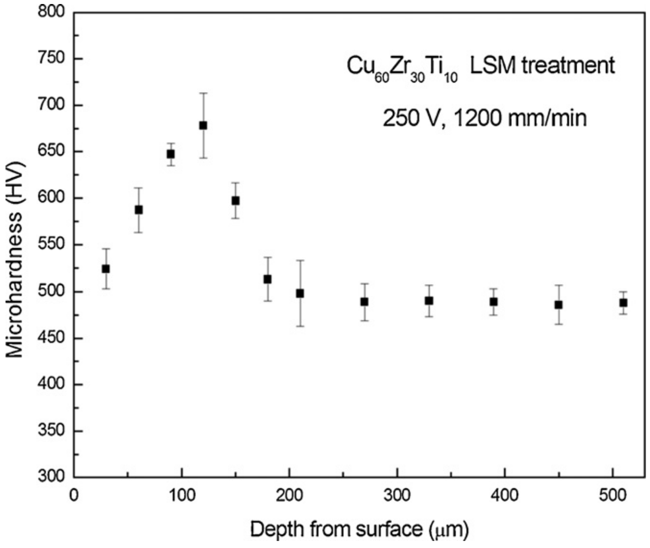

Fig. 6. Microhardness depth profile of the laser surface treated $Cu_{60}Zr_{30}Ti_{10}$ alloy.

Table 2
Physical and thermal properties of $Cu_{60}Zr_{30}Ti_{10}$ glassy alloy used in thermal simulation.

Density ρ (kg/m^3)	Thermal conductivity k (W/m K)	Convective heat transfer h (W/m^2 K)	Emissivity for thermal radiation ε	Specific heat C_p (J/kg K)	Laser powder density P_d (W/m^2)
7.3	9 at 300 K [27] 20 at 734 K [28]	2000 [29]	0.4 [26]	340 [30]	3.5×10^8

The microhardness depth profile of the $Cu_{60}Zr_{30}Ti_{10}$ alloy treated at 250 V and 1200 mm/min is shown in Fig. 6. The hardness firstly increases with the increase in depth until about 120 μm and then gradually decreases to the hardness of the substrate. The hardening of the alloy in the depth range of 0–120 μm is attributed to the decrease in free volume of the relaxed amorphous phase and the precipitation of hard intermetallics. The highest hardness (650 HV) measured at about 120 μm in depth is in the transitional layer B. The gradual drop in hardness from 120 μm depth is due to the existence of coarse crystals. The hardness depth profile also reflects the evolution of the gradient structure for the treated Cu-based alloy.

For a better understanding of the formation mechanism of the gradient structure in the laser treated $Cu_{60}Zr_{30}Ti_{10}$ alloy, finite volume method was used to simulate the process of laser surface melting with super high heating/cooling rates. At the alloy surface, the heat balance between the laser power absorbed by the sample and the radiation losses obeys the equations reported in Ref. [26]. The thickness of the rectangular specimen is 2 mm. The surfaces except for the top one are considered thermally insulated. The laser processing parameters and the relevant physical and thermal properties of the alloy are listed in Table 2.

In this model, a single laser pulse is employed and the treated surface is regarded as a homogeneous target. Heat transfers through conductivity, convection and radiation. The acting time (t_p) of a laser pulse is 1 ms and three different timing scenes at 0.5 ms, 1 ms and 5 ms, which correspond to the stages of heating, heating end and cooling, respectively, are investigated. Fig. 7(a–c) shows the temperature distributions at the top surface and the cross section of the $Cu_{60}Zr_{30}Ti_{10}$ alloy treated at the working voltage of 250 V and the scanning speed of 1200 mm/min. At 0.5 ms, the peak temperature is 1550 K and the thickness of the heat affected zone is about 170 μm. When the pulse ends at 1 ms, the peak temperature increases to 2400 K, which is much higher than the melting temperature of $Cu_{60}Zr_{30}Ti_{10}$ alloy. At 5 ms, the temperature of the top surface is 960 K and the heat affected zone is as thick as 560 μm. The heating/cooling profiles of the layers at different depths are presented in Fig. 7(d). It is seen that, at 10 ms, the temperature has already decreased below the T_g of $Cu_{60}Zr_{30}Ti_{10}$ alloy (724 K) [31]. It indicates that the cooling rate is in the order of 10^5 K/s and the surface vitrification is thermodynamically achievable.

From Fig. 7(d), it can be seen that the top surface experiences the highest peak temperature and the highest heating and

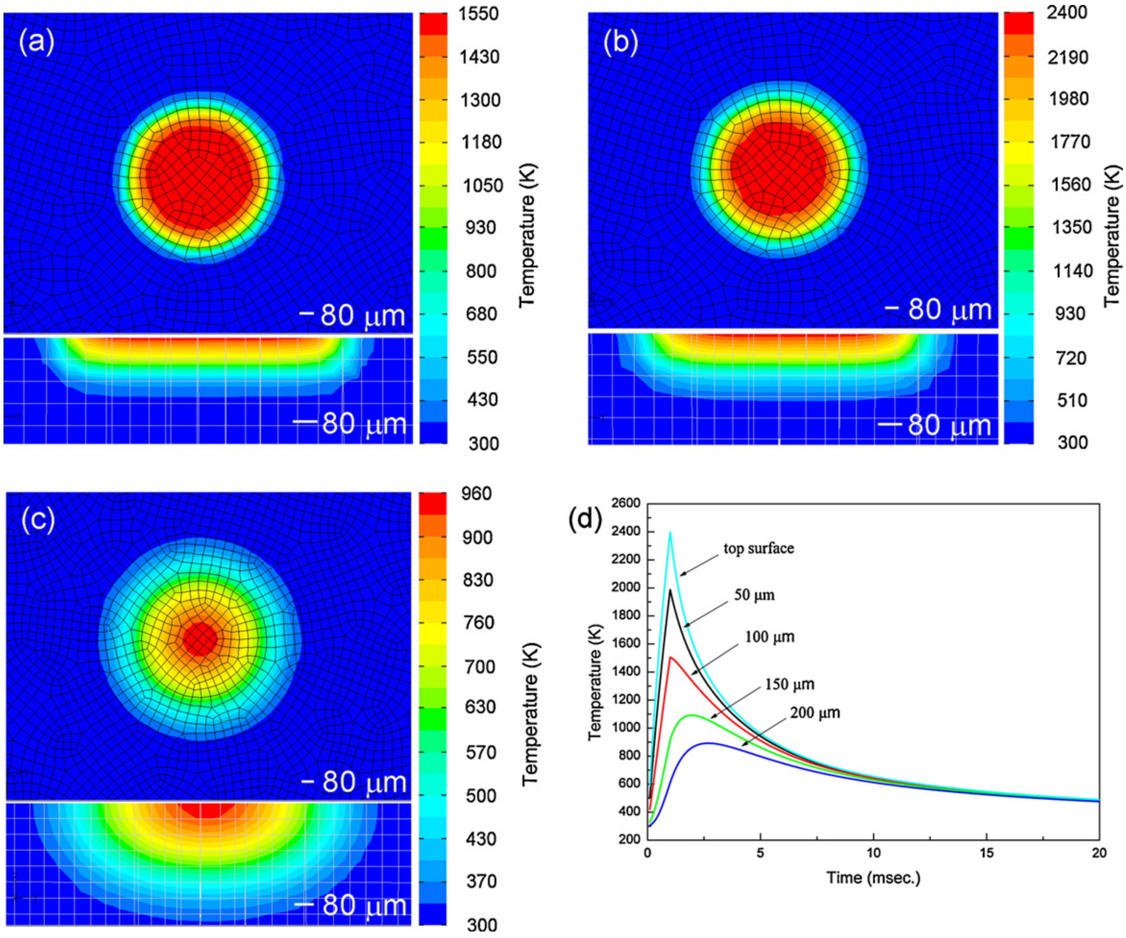

Fig. 7. Finite volume simulation results including the temperature distributions on the top surface and the cross-section of the laser surface treated $Cu_{60}Zr_{30}Ti_{10}$ alloy (250 V, 1200 mm/min) at (a) 0.5 ms, (b) 1 ms and (c) 5 ms, and (d) the temperature profiles of different layers.

cooling rates. The peak temperature and heating/cooling rates gradually recede with increasing depth from the top surface. The peak temperature at 100 μm depth (1500 K) is higher than the melting temperature of $Cu_{60}Zr_{30}Ti_{10}$ alloy (T_m = 1106 K), while that at 150 μm (1100 K) is lower than the T_m. Accordingly, it is concluded that the thickness of the melted surface layer is in the range of 100–150 μm with the present processing parameters. The simulated results agree well with the SEM observations shown in Fig. 3(b), though the melted zone observed is a little thicker because of the thermal interactions between the neighboring laser spots [32]. As discussed above, the transitional layer B locating in the depth range of 100–150 μm can involve the liquid–solid two-phase region (T_l = 1175 K and T_m = 1106 K) [31]. In this region, the phases with lower melting temperature of $Cu_{60}Zr_{30}Ti_{10}$ alloy can be melted; however, the solid phases including intermetallics ($Cu_{10}Zr_7$) [33] with higher melting temperatures were reserved, leading to a semi-solid state. The melted phases were rapidly quenched to form the amorphous phase. The unmelted solid phases were broken and stirred by the heat current transferred from the upper layers and randomly distributed in the matrix as shown in Fig. 5(b). In transitional layer A, though the peak temperature is higher than the liquidus temperature of the alloy, the phases with higher liquidus temperatures could not be melted completely and transitorily remained in the liquid phase due to the very limited heating duration (1 ms). Moreover, in the process of laser surface melting, oxidation may happen and the single phase oxide particles with high melting temperatures would also exist in the melted alloy. These residual infusible tiny cells and particles could be the nucleus of heterogeneous nucleation and ultrafine crystallites would precipitate and distribute in amorphous matrix.

4. Conclusions

Glass formation by laser surface melting is related to the GFA and melting temperatures of the alloys as well as the compositional inhomogeneity and microstructural nonuniformity. Amorphous surfaces were formed for $Zr_{55}Al_{10}Ni_5Cu_{30}$, $Zr_{48}Cu_{40}Al_{10}Y_2$, and $Cu_{60}Zr_{30}Ti_{10}$ alloys with high GFA after laser melting. The laser treated $Cu_{64}Zr_{36}$, $Al_{86}Si_{0.5}Ni_{4.06}Co_{2.94}Y_6Sc_{0.5}$, and $[(Fe_{0.5}Co_{0.5})_{0.75}B_{0.2}Si_{0.05}]_{96}Nb_4$ alloys with low GFA/high melting temperature exhibited amorphous–crystalline composite structures on the surface. For the $Cu_{60}Zr_{30}Ti_{10}$ alloy, fast scanning speeds and proper high working voltages are beneficial to the glass formation. The laser surface treated $Cu_{60}Zr_{30}Ti_{10}$ alloy exhibits gradient structure including amorphous surface, amorphous–crystalline composites transitional region and crystalline substrate, and the transitional layer B with amorphous–dendrite composite structure shows the highest microhardness. Simulation of the peak temperatures and heating/cooling rates of the layers at different depths from the top surface was performed, and the simulated and experimental results indicate that the formation mechanism of the gradient structure is related to the heating/cooling profiles during the laser surface treatment as well as the effect of heterogeneous nucleation caused by the substrate.

Acknowledgements

This work was financially supported by the National Basic Research Program of China (2007CB613900), the National Nature Science Foundation of China (50771005 and 50771006) and Program for New Century Excellent Talents in University (NCET-07-0041).

References

[1] A.L. Greer, Science 267 (1995) 1947.
[2] A. Inoue, Acta Mater. 48 (2000) 279.
[3] T. Zhang, A. Inoue, T. Masumoto, Mater. Trans. 32 (1991) 1005.
[4] S.J. Pang, T. Zhang, K. Asami, A. Inoue, Corros. Sci. 44 (2002) 1847.
[5] F. Audebert, R. Colaco, R. Vilar, H. Sirkin, Scripta Mater. 48 (2003) 281.
[6] A. Inoue, Bulk Amorphous Alloys, Trans Tech Publications, Zurich, 1998.
[7] N. Kumagai, K. Asami, K. Hashimoto, J. Non-Cryst. Solids 87 (1986) 123.
[8] Y. Yang, J.D. Hu, H.Y. Wang, S.Y. Liu, Y.X. Li, Z.X. Guo, Mater. Lett. 60 (2006) 1128.
[9] K. Asami, T. Sato, K. Hashimoto, J. Non-Cryst. Solids 68 (1984) 261.
[10] B.Q. Chen, S.J. Pang, P.P. Han, Y. Li, A.R. Yavari, G. Vaughan, T. Zhang, J. Alloys Compd. 504S (2010) S45.
[11] B.Q. Chen,Y. Li, R. Li, S.J. Pang, Y. Cai, H. Wang, T. Zhang, J. Mater. Res., in press.
[12] D.T.A. Matthews, V. Ocelĭık, J.Th.M. de Hosson, Mater. Sci. Eng. A 471 (2007) 155.
[13] D.T.A. Matthews, V. Ocelík, J.Th.M. de Hosson, J. Mater. Res. 22 (2007) 460.
[14] X.L. Wu, Y.S. Hong, Surf. Coat. Technol. 141 (2001) 141.
[15] T.M. Yue, Y.P. Su, H.O. Yang, Mater. Lett. 61 (2007) 209.
[16] X. Wu, B. Xu, Y. Hong, Mater. Lett. 56 (2002) 838.
[17] J. Luo, H. Duan, C. Ma, et al., Mater. Trans. JIM 47 (2006) 450.
[18] J.Y. Fu, Master Thesis. Beihang University, Beijing, 2007.
[19] D.H. Xu, B. Lohwongwatana, G. Duan, W.L. Johnson, Acta Mater. 52 (2004) 2621.
[20] A. Inoue, W. Zhang, T. Zhang, K. Kurosaka, Acta Mater. 49 (2001) 2645.
[21] A. Inoue, B.L. Shen, C.T. Chang, Intermetallics 14 (2006) 936.
[22] L.C. Zhuo, S.J. Pang, H. Wang, T. Zhang, Chin. Phys. Lett. 26 (2009) 066402.
[23] H.W. Yang, P. Dong, J.Q. Wang, Y. Li, Mater. Sci. Eng. A 449–451 (2007) 273.
[24] T. Chande, J. Mazumder, Appl. Phys. Lett. 41 (1982) 42.
[25] B. Li, Z.Y. Li, J.G. Xiong, L. Xing, D. Wang, Y. Li, J. Alloys Compd. 413 (2006) 118.
[26] A. Basu, A.N. Samant, S.P. Harimkar, J. Dutta Majumdar, I. Manna, N.B. Dahotre, Surf. Coat. Technol. 202 (2008) 2623.
[27] X.J. Han, H. Teichler, Phys. Rev. E 75 (2007) 061501.
[28] M. Yamasaki, S. Kagao, Y. Kawamura, Scripta Mater. 53 (2005) 63.
[29] C.C. Aydiner, E. Üstündag, M.B. Prime, A. Peker, J. Non-Cryst. Solids 316 (2003) 82.
[30] Y.K. Kuo, K.M. Sivakumar, et al., Phys. Rev. B 74 (2006) 014208.
[31] E.S. Park, H.J. Chang, D.H. Kim, T. Ohkubo, K. Hono, Scripta Mater. 54 (2006) 1569.
[32] J. Kim, D. Lee, S. Shin, C. Lee, Mater. Sci. Eng. A 434 (2006) 194.
[33] ASM Alloys Phase Diagram Center, http://www.asminternational.org/asmenterprise/apd.